





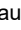




RESEARCH ARTICLE | SEPTEMBER 18 2023

Growth and optical properties of NiO thin films deposited by pulsed dc reactive magnetron sputtering

Special Collection: [Celebrating the Achievements and Life of Joe Greene](#)

Faezeh A. F. Lahiji ; Samiran Bairagi ; Roger Magnusson ; Mauricio A. Sortica ;
Daniel Primetzhofer ; Erik Ekström ; Biplab Paul ; Arnaud le Febvrier ; Per Eklund 



J. Vac. Sci. Technol. A 41, 063402 (2023)

<https://doi.org/10.1116/6.0002914>



CrossMark

Growth and optical properties of NiO thin films deposited by pulsed dc reactive magnetron sputtering

Cite as: J. Vac. Sci. Technol. A 41, 063402 (2023); doi: 10.1116/6.0002914

Submitted: 26 June 2023 · Accepted: 17 August 2023 ·

Published Online: 18 September 2023



Faezeh A. F. Lahiji,^{1,a)} Samiran Bairagi,¹ Roger Magnusson,¹ Mauricio A. Sortica,² Daniel Primetzhofer,^{2,3} Erik Ekström,¹ Biplab Paul,¹ Arnaud le Febvrier,¹ and Per Eklund¹

AFFILIATIONS

¹Thin Film Physics Division, Department of Physics, Chemistry and Biology (IFM), Linköping University, Linköping, SE 58183, Sweden

²Tandem Laboratory, Uppsala University, Uppsala, SE 75120, Sweden

³Division of Applied Nuclear Physics, Department of Physics and Astronomy, Uppsala University, Uppsala, SE 75120, Sweden

Note: This paper is part of the Special Topic Collection Celebrating the Achievements and Life of Joe Greene.

a)Electronic mail: faezech.alijan.farzad.lahiji@liu.se

ABSTRACT

NiO thin films with varied oxygen contents are grown on Si(100) and c-Al₂O₃ at a substrate temperature of 300 °C using pulsed dc reactive magnetron sputtering. We characterize the structure and optical properties of NiO changes as functions of the oxygen content. NiO with the cubic structure, single phase, and predominant orientation along (111) is found on both substrates. X-ray diffraction and pole figure analysis further show that NiO on the Si(100) substrate exhibits fiber-textured growth, while twin domain epitaxy was achieved on c-Al₂O₃, with NiO(111) || Al₂O₃(0001) and NiO[110] || Al₂O₃[1010] or NiO[110] || Al₂O₃[2110] epitaxial relationship. The oxygen content in NiO films did not have a significant effect on the refractive index, extinction coefficient, and absorption coefficient. This suggests that the optical properties of NiO films remained unaffected by changes in the oxygen content.

© 2023 Author(s). All article content, except where otherwise noted, is licensed under a Creative Commons Attribution (CC BY) license (<http://creativecommons.org/licenses/by/4.0/>). <https://doi.org/10.1116/6.0002914>

I. INTRODUCTION

Nickel oxide, NiO, has been studied extensively for its magnetic,^{1–3} electronic,^{4–6} thermoelectric,^{7–9} and optical^{5,10–12} properties. Bulk NiO has a cubic (NaCl) structure with a lattice parameter of 4.195 Å. It is a p-type semiconductor^{13,14} with a bandgap in the range of 3.5–4.0 eV, antiferromagnetic below 523 K, and remains a Mott–Hubbard insulator¹⁵ above the Néel temperature. NiO is an established material in a wide range of applications¹⁶ like transparent conductors in smart windows,^{17,18} photovoltaics,^{19,20} chemical sensors,^{21–23} and resistive random-access memories,^{23–27} in many cases as thin films.

The electrical and optical properties of NiO thin films are strongly dependent on process parameters such as substrate temperature^{28–30} and oxygen content,^{31,32} as well as the type of the deposition method.^{31–39} Nickel oxide thin films with varied oxygen to nickel ratios (Ni_{1-x}O) and multiple nickel valence

states^{11,14,32,36,40–42} have been investigated. The oxidation state of Ni is a key factor for the physical properties and the stoichiometry of NiO thin film. The effect on optical properties can be observed already by ocular inspection; the color is an indication of the stoichiometry of NiO thin films.¹¹ Pure stoichiometric NiO is pale green, and nonstoichiometric NiO is dark gray.

For the thin-film synthesis of nickel oxide, a range of methods can be used: chemical vapor deposition,³³ atomic layer deposition,¹² pulsed laser deposition,³⁵ solgel deposition,³⁴ thermal evaporation,³⁷ and magnetron sputtering. In particular, sputter-deposition has several advantages over other vacuum coating techniques. It is a versatile method used for the development of a large number of commercial applications from microelectronic fabrication to decorative coatings. Direct-current (dc)³² and radio-frequency (rf) reactive magnetron sputtering¹⁴ as well as high power impulse magnetron sputtering (HiPIMS)³⁸ are sputter-deposition techniques that have

18 March 2024 15:19:20

been used for nickel oxide growth. Nevertheless, there is still a need to determine the effects of processing parameters and growth mode on the structural, optical, and electrical properties of NiO thin films.

In the present work, we investigate the effect of stoichiometry of NiO thin films. We focus on the effect of deposition conditions like oxygen flow ratio on the structure of NiO thin films grown on Si(100) and c-plane sapphire and the effect on optical properties.

II. EXPERIMENTAL DETAILS

Nickel oxide films were deposited on the sapphire substrate (Al_2O_3) (c-plane) and (100) oriented silicon substrate with a native oxide with a size of $10 \times 10 \text{ mm}^2$. Prior to deposition, the substrates were cleaned sequentially with acetone and isopropanol in an ultrasonic bath for 5 min and blow-dried with nitrogen gas. After mounting the samples on a rotatable substrate holder, the deposition chamber was evacuated to a base pressure of $3 \times 10^{-6} \text{ Pa}$. Details of the deposition system can be found elsewhere.⁴³

The NiO films were deposited using a Ni target 50 mm (2 in.) in diameter (99.99% purity). To investigate the influence of the oxygen flow ratio on the structure and properties of the deposited films, the $\text{O}_2/(\text{Ar} + \text{O}_2)$ gas flow ratio (i.e., the flow of O_2 divided by the total gas flow) was varied from 4% to 51% for the series of depositions with the fixed total gas flow at 45 SCCM. The partial pressure of the total gas used for deposition corresponds to 0.3 Pa (2.5 mTorr). Before each deposition, the nickel target was presputtered in an argon atmosphere for 2 min to remove any contamination on the surface while the substrates were shielded with a shutter to prevent the deposition of Ni on them. The substrates were preheated for 15 min to obtain a stable temperature. Each deposition was carried out for 30 min while keeping all parameters constant, which resulted in a thickness ranging from ~50 to 490 nm depending on the oxygen flow. The deposition process was carried out by pulsed dc reactive magnetron sputtering. A bipolar pulsed dc power supply with 150 W, and a frequency of 100 KHz was used to generate plasma. The duty cycle was varied between 90%, with 1 μs reverse time for the low oxygen flow ratio, and 80% with a reverse time of 2 μs for the higher oxygen flow ratio in order to reduce arcing.

To assess the chemical composition of the films, we employed an approach combining Rutherford backscattering spectrometry (RBS) and heavy-ion elastic recoil detection analysis (HIERDA). Experiments were performed by employing a 5MV 15-SDH2 pelletron accelerator at Uppsala University, as described by Ström *et al.*⁴⁴ For HIERDA, we employed a primary beam of 36 MeV I^{8+} ions, which created recoils, detected in a time-of-flight telescope terminated by an energy dispersive detector.⁴⁵ The beam incidence and the recoil detection angle were 22.5 with respect to the sample surface, resulting in a recoil detection angle of 45°. HIERDA revealed the films to be composed of high purity NiO_x with contaminations of H, C, and Ar not exceeding a few per mille atomic fraction. The ratio of nickel to oxygen was furthermore assessed by Rutherford backscattering spectrometry, employing a primary beam of 2 MeV He^+ primary ions. Spectra were analyzed using the SIMNRA simulation package.⁴⁶

X-ray diffraction (XRD) θ - 2θ scans were carried out in a PANalytical X'Pert PRO diffractometer system equipped with a $\text{Cu K}\alpha$ source and operated at 45 kV and 40 mA using a

Bragg-Brentano configuration. The incident optics were a 0.5° divergence slit and a 0.5° antiscatter slit, and the diffracted beam included a 5.0 mm antiscatter slit and 0.04 rad Soller slits and a Ni filter (to filter $\text{CuK}\beta$ radiation). The PreFIX stage was set to continuous scanning and spinner mode. Step sizes and counting times per step were 0.0084° and 15.240 s, respectively. Pole figure measurements were performed with an x-ray diffractometer (Malvern Panalytical Empyrean) in a configuration using a zero setpoint crossed slit as the primary optics and a parallel plate collimator (0.27°) as the secondary optic. The collection time was 1.0 s/step, and a step size of 2.50° was chosen to acquire data for pole figure measurements along rotation (φ) and tilt (Ψ) directions in the range from 0° to 360° and from 0° to 85°, respectively.

A scanning electron microscope (SEM Leo 1550 Gemini, Zeiss) operated with an acceleration voltage of 12 kV and an in-lens detector was used to observe the surface morphology.

A Mueller matrix spectroscopic ellipsometer from J.A. Woollam Co, Inc. was used to measure samples over a spectral range of 210–1600 nm (0.7–5.9 eV) at four angles of incidence from 45° to 75° in steps of 10°. CompleteEASE® modeling software, also from J. A. Woollam Co., Inc., version 5.21, was used for the analysis and model fitting of acquired optical data. The optical properties such as the complex refractive index $N(\lambda) = n(\lambda) + ik(\lambda)$, where n and k represent the refractive index and the extinction coefficient, respectively, and the absorption coefficient $\alpha(\lambda)$ was obtained from the model fitting of ellipsometric data, along with film thickness and surface roughness values. The fitting procedures that were used to extract the optical constant of the NiO film, include a general oscillator model consisting of Cody-Lorentz and PSemi oscillators near the bandgap region and two Gaussian oscillators at higher photon energies.

III. RESULTS AND DISCUSSION

The results measured by RBS for NiO on Si(100) and c- Al_2O_3 are summarized in Table I. The stoichiometry of $\text{NiO}_x = 1$ in the film occurs for the lowest percentage of the O_2 flow ratio. By increasing the percentage of the O_2 flow ratio in the overall gas flow, the oxygen content exceeds the stoichiometric content. While keeping the duration of deposition constant, the thickness of the NiO film was altered by adjusting the oxygen flow in the total gas flow, resulting in a decrease from 490 to ~50 nm as the oxygen flow ratio was increased in the total gas flow.

A. Structural characterization

Figure 1(a) shows the θ - 2θ XRD patterns of the NiO_x films deposited on the Si(100) substrate at 300 °C with O content variation in the film. The Si substrate peaks are observed at $2\theta = 32.9^\circ$ and $2\theta = 69.3^\circ$. The diffraction pattern shows the presence of the 111 and 222 peaks of cubic NiO at 37.2° and 79.3° for all samples. The XRD deposited the highest oxygen content ($\text{NiO}_{1.30}$) only showing the 111 and 222 peaks with $4.227 \pm 0.004 \text{ \AA}$. In addition to the 111 peak and 222 with lower intensity (compared to the XRD peak for the film at high oxygen content), the 200 peak is also observed for intermediate oxygen composition ($\text{NiO}_{1.28}$ and $\text{NiO}_{1.12}$). For the films with the lower oxygen content in the film ($\text{NiO}_{1.06}$ to $\text{NiO}_{0.99}$), 220 and 311 peaks are observed together with

18 March 2024 15:19:20

TABLE I. Composition and thickness of NiO_x films estimated by RBS.

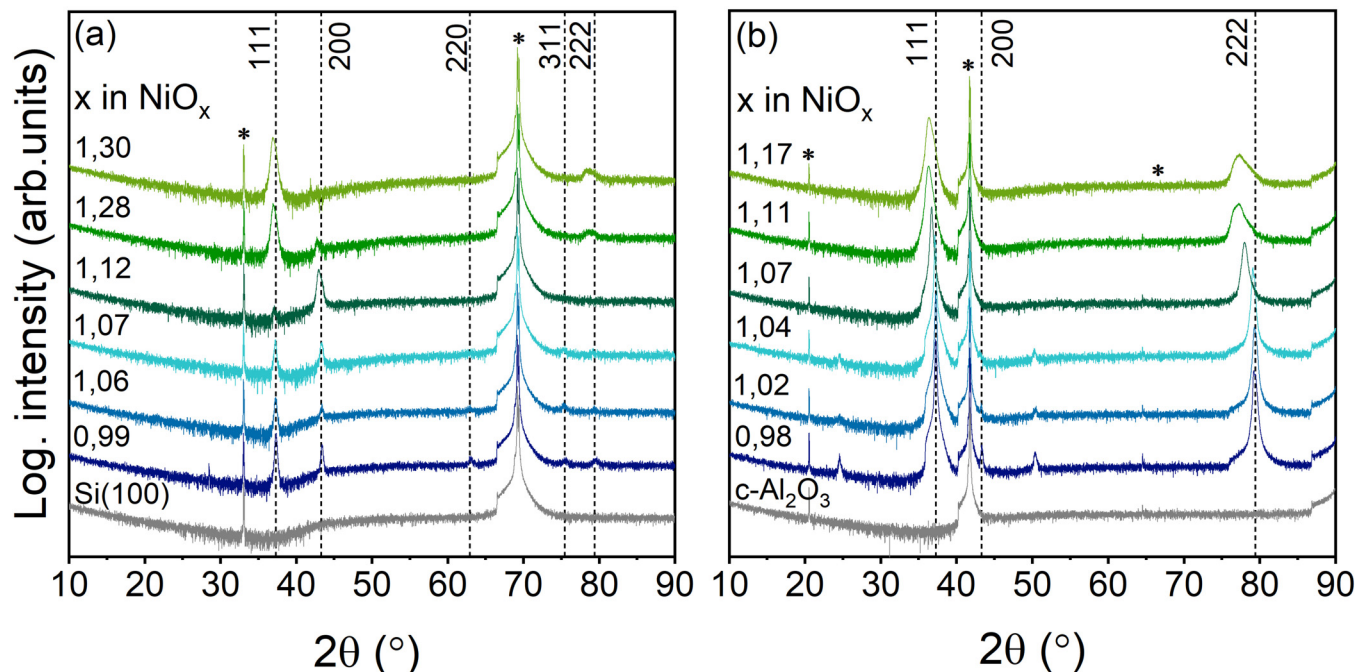
Percentage of O ₂ (%) flow ratio in the total gas flow	Composition from RBS (%)						Reduced name NiO _x	
	Si substrate		c-Al ₂ O ₃ substrate		Thickness (nm)		Si	c-Al ₂ O ₃
	Ni	O	Ni	O	Si	c-Al ₂ O ₃		
4	50.2	49.8	50.3	49.7	489	492	NiO _{0.99}	NiO _{0.98}
19	48.3	51.6	49.3	50.7	348	348	NiO _{1.06}	NiO _{1.02}
27	48.3	51.7	49.0	51.0	230	229	NiO _{1.07}	NiO _{1.04}
35	47.0	53.0	48.2	51.8	81	82	NiO _{1.12}	NiO _{1.07}
43	43.8	56.2	47.3	52.7	54	52	NiO _{1.28}	NiO _{1.11}
51	43.3	56.7	46.0	54.0	43	51	NiO _{1.30}	NiO _{1.17}

111, 222, and 200 peaks identified as the cubic NiO phase with lattice parameters of 4.175 ± 0.004 Å (NiO_{1.06}) and 4.179 ± 0.004 Å (NiO_{0.99}). See Fig. S1 in the supplementary material⁵³ for the evolution of the lattice parameter on the Si(100) substrate.

XRD patterns of films deposited with the same set of conditions on c-Al₂O₃ are shown in Fig. 1(b). Except for the substrate peak situated at $2\theta = 20.7^\circ$ and $2\theta = 41.7^\circ$, the XRD patterns are dominated by the 111 and 222 diffraction peaks at 36.4° and 77.5° with lattice parameters of 4.275 ± 0.004 Å for the films with the highest oxygen content (NiO_{1.17}). The NiO 222 peak intensity increases with decreasing the amount of oxygen for the films

NiO_x, $x = 1.07$ and is shifted to higher angles (79.90°). The strong and sharp peaks indicate that the NiO films are highly preferentially orientated regardless of the oxygen composition. For the films with lower oxygen content, (NiO_{1.04}) with 4.187 ± 0.004 Å, (NiO_{1.02}) with 4.179 ± 0.004 Å, and (NiO_{0.98}) with 4.189 ± 0.004 Å, the 200 peak is detected where its intensity is increasing with decreasing oxygen content. See Fig. S1 in the supplementary material⁵³ for the evolution of the lattice parameter on the c-Al₂O₃ substrate.

Furthermore, an additional peak is observed in the x-ray diffraction patterns of NiO_{0.99} on the Si(100) substrate, appearing at



18 March 2024 15:19:20

FIG. 1. θ - 2θ XRD patterns of the NiO_x films deposited with varying oxygen contents in the film on (a) Si(100) and (b) c-Al₂O₃ substrates at 300 °C. Substrate peaks are marked with *.

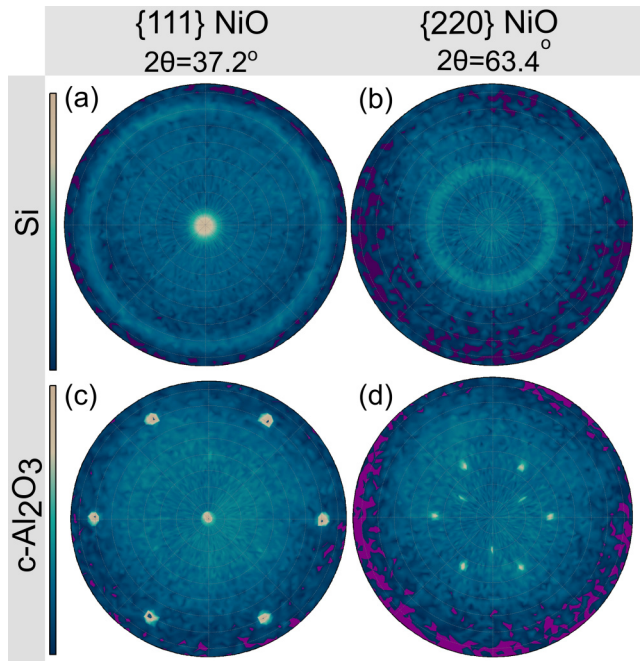


FIG. 2. {111} and {220} pole figures for NiO thin films on (a) and (b) Si(100) and (c) and (d) c-Al₂O₃ substrates.

an angle of $\sim 28.5^\circ$. Similarly, for the last three samples, NiO_{1.04}, NiO_{1.02}, and NiO_{0.98} on the c-Al₂O₃ additional peak is observed at angles of $\sim 24.5^\circ$ and 50.36° . These additional peaks cannot be attributed to either NiO_x or Ni metal based on the available data in

our database. This might suggest the possible presence of other crystalline phases or impurities in these samples.

Figure 2 shows the poles figures measured for $2\theta = 37.28^\circ$ (NiO 111 peak) and for $2\theta = 62.91^\circ$ (220 of NiO) measured on the films deposited with the highest oxygen content NiO_{1.17} in Fig. 2(a) Si(100) and Fig. 2(b) c-Al₂O₃. The presence of a diffraction spot in the center of pole figure 111 and a ring at $\Psi = 35^\circ$ on the {220} pole figure reveals a fiber texture growth of NiO along its [111] direction on the Si(100) substrate. In addition to the main pole intensity at the center of the {111} pole figure [Fig. 2(c)], both {111} and {220} pole figures display intensity maxima with three-fold symmetry on the c-Al₂O₃ substrate. The presence of six peaks, rather than three, is due to the formation of twin domains on the c-Al₂O₃ surface. This is evidence that NiO was grown epitaxially on c-Al₂O₃, with the epitaxial relation NiO(111) \parallel Al₂O₃(0001) and NiO[110] \parallel Al₂O₃[1010] or NiO[110] \parallel Al₂O₃[2110].

Figure 3 shows the SEM micrographs of the films deposited on Si(100) and c-Al₂O₃ substrates with different oxygen compositions in the film. The films deposited on the Si(100) substrate with high oxygen content NiO_{1.30}, NiO_{1.28} had smooth, uniform, and compact surfaces with distinct grain boundaries. However, a noticeable change in the morphology was observed in the NiO_{1.12} sample, where the surface became irregular, with flat and flaky grains oriented in different directions. As the oxygen content continued to decrease, NiO_{1.07}, NiO_{1.06}, and NiO_{0.99}, the growth and the arrangement of the grains are affected, resulting in larger grains with different structures and orientations.

A smooth, uniform, and closely packed with pyramidal shape grains were observed for the films deposited on c-Al₂O₃ with high oxygen content, NiO_{1.17}, NiO_{1.11}, and NiO_{1.07}. A significant change started with decreasing oxygen incorporation. Films deposited with low oxygen content NiO_{1.04}, NiO_{1.02}, and NiO_{0.98} exhibited rough surface triangular pyramids and large grains.

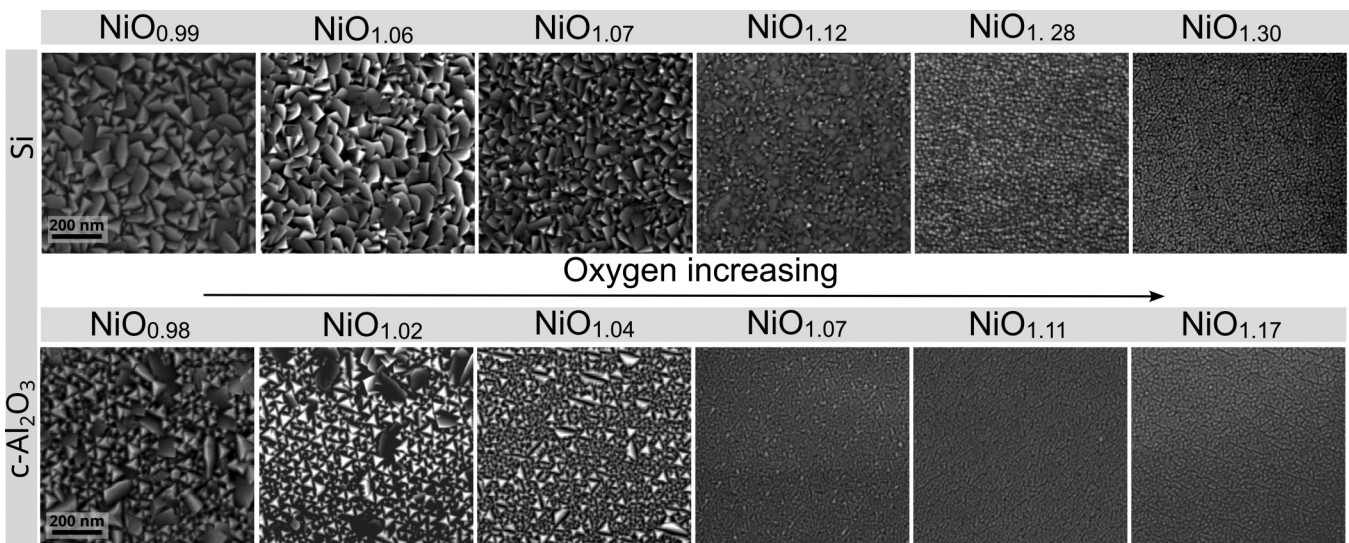


FIG. 3. Scanning electron microscopy (SEM) images of NiO_x films deposited with varying oxygen contents from Si(100), and c-Al₂O₃ at 300 °C.

18 March 2024 15:19:20

B. Optical properties

In order to gain a deeper understanding of the relationship between the oxygen composition and the optical properties of NiO_x films, spectroscopic ellipsometry was employed to investigate the optical characteristics. The optical properties were measured on the $c\text{-Al}_2\text{O}_3$ substrate with better crystalline quality and preferred crystallographic orientation. The optical properties of deposited NiO_x films on the $c\text{-Al}_2\text{O}_3$ substrate were modeled using a general oscillator model consisting of Cody-Lorentz and PSemi oscillators near the bandgap region and two Gaussian oscillators at higher photon energies. The model was able to accurately represent the optical properties of the film within a certain range of photon energies 0.73–5.9 eV.

The refractive index (n) and extinction coefficient (k) of the investigated films are extracted from the spectroscopic ellipsometry data Ψ and Δ , which yield the complex of refraction,

$$N = n + ik. \quad (1)$$

The absorption coefficient (α) varies with the extinction coefficient (k) through the following formula:

$$\alpha = 4\pi k/\lambda,$$

where λ is the wavelength of the incident light. The optical energy gap (E_g) is determined using the Tauc and Davis–Mott relation, given by the following equation:

$$\alpha h\nu = A(h\nu - E_g)^n,$$

where h is the Planck constant, ν is the incident photon's frequency, and A is an energy-independent constant. The exponent n depends on the type of electron transition in the bandgap region, taking a value of 1/2 for allowed direct and 2 for allowed indirect interband transitions. See Fig. S2 in the supplementary material⁵³ for the plots providing detailed information and analysis of each individual sample of NiO_x films deposited on the $c\text{-Al}_2\text{O}_3$ substrate with different oxygen contents. The optical direct bandgap is estimated by linearly extrapolating the Tauc plot and determining its intersection with the $(h\nu)$ -axis.⁴⁷

The optical constants n and k of NiO_x on the $c\text{-Al}_2\text{O}_3$ substrate, as a function of photon energy, are shown in Figs. 4(a) and 4(b). The refractive index (n), as depicted in Fig. 4(a), indicates a slight variation within the range of approximately ~ 2.39 – ~ 2.36 as the oxygen content decreases in the NiO_x films on the $c\text{-Al}_2\text{O}_3$ substrate. See Fig. S3(c) in the supplementary material⁵³ for the variation in the refractive index at 630 nm and the extinction coefficient at 630 nm with varying oxygen contents. This change in the refractive index (n) at 2 eV photon energy aligns well with the previously reported¹² refractive index value of 2.37 for the NiO film on the Si substrate at the same photon energy. Furthermore, the film with intermediate oxygen content, $\text{NiO}_{1.07}$, exhibits the highest refractive index, which may correspond to the film's optical density and structure. The extinction coefficient (k) for the NiO_x films on the $c\text{-Al}_2\text{O}_3$ substrate remains close to zero showing only a slight change from 0.06 to 0.01 as depicted in Fig. 4(b).

Figure 5 displays the existence of direct $(\alpha h\nu)^2$ transition for the as-deposited NiO_x films versus photon energy (eV), and Fig. 5(b) shows the variation in the bandgap energy (E_g) as a function of oxygen content for all NiO_x samples.

The extrapolated values of the linear part for the direct bandgap versus photon energy (eV) in Fig. 5(a) are shown in Fig. 5(b), plotted versus the oxygen content for each NiO_x film. The results indicate that the direct bandgap energy shows only a slight variation with changing oxygen content. Films with higher oxygen content, such as $\text{NiO}_{1.17}$, $\text{NiO}_{1.11}$, and $\text{NiO}_{1.07}$, exhibit a direct bandgap energy of around 3.65 eV. As the oxygen content

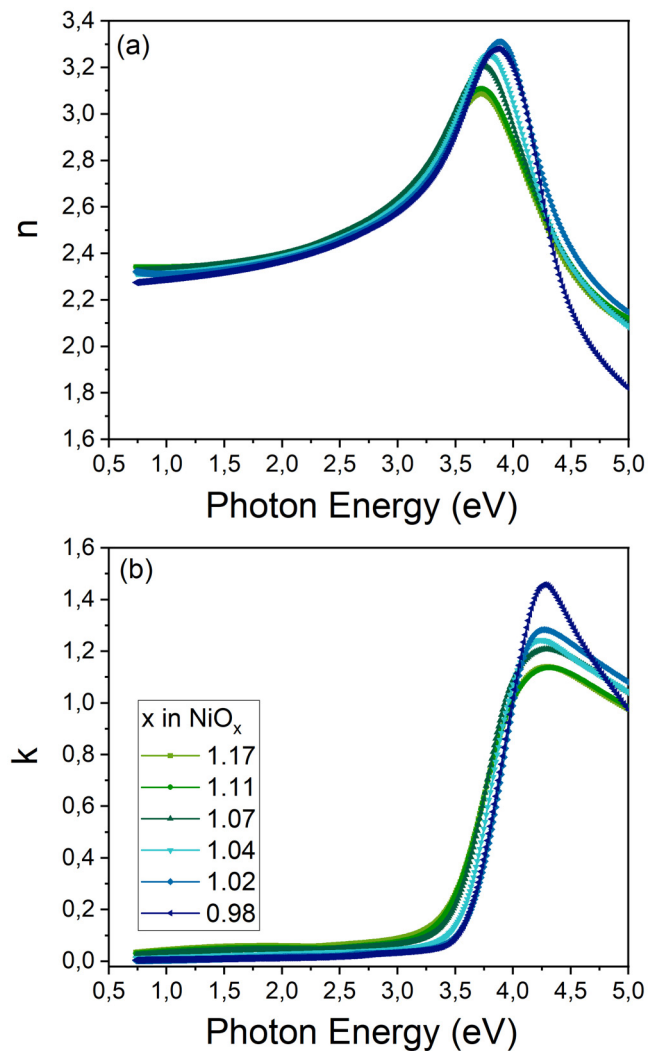


FIG. 4. (a) Refractive index (n) and (b) extinction coefficient (k) vs photon energy (eV) [and see Figs.S3(a) and S3(b) in supplementary material⁵³ for (a) Refractive index (n) and (b) extinction coefficient (k) vs wavelength (nm)] for NiO_x films deposited on the $c\text{-Al}_2\text{O}_3$ substrate with varying oxygen contents.

18 March 2024 15:19:20

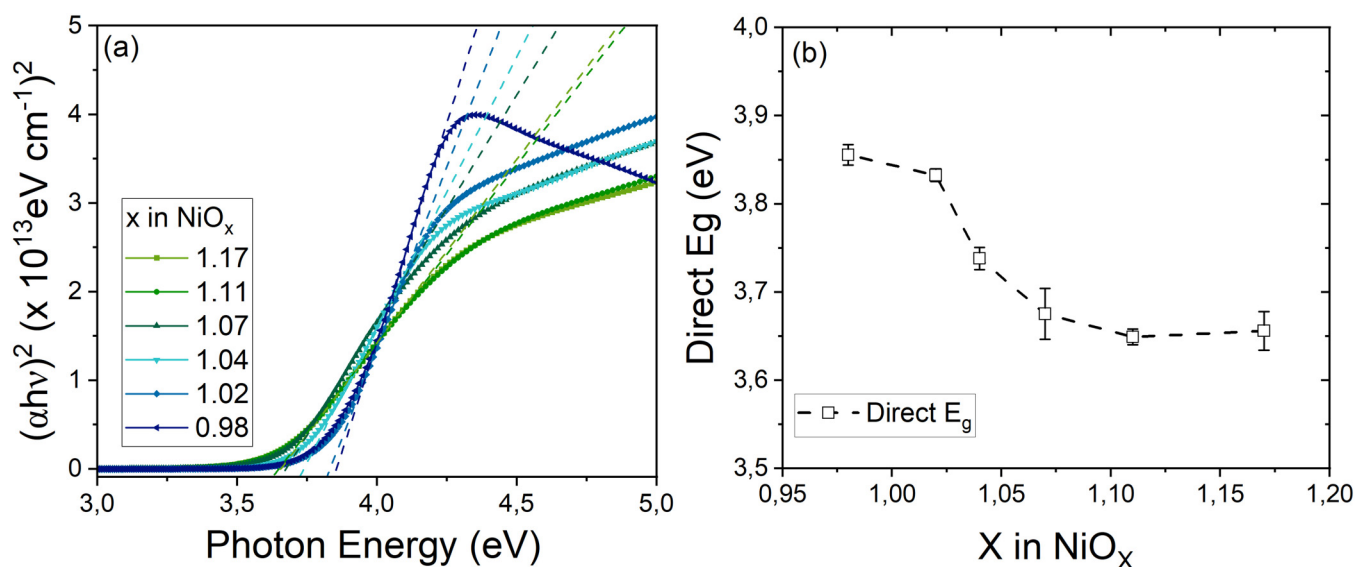


FIG. 5. Plots (a) show the linear extrapolation of $(\alpha h\nu)^2$ for the direct bandgap energy vs photon energy (eV), and (b) is the variation in the extrapolated direct bandgap values with varying oxygen contents for NiO_x films deposited on c- Al_2O_3 at 300 °C.

decreases, the bandgap energy slightly increases, up to 3.85 eV for films such as $\text{NiO}_{1.04}$, $\text{NiO}_{1.02}$, and $\text{NiO}_{0.982}$. However, it is important to note that the change in the bandgap is not significant despite the variation in oxygen content. The reported bandgap energy value for nickel oxide falls within the range of 3.4–4.0 eV,^{12,47} which is consistent with our findings.

The refractive index, extinction coefficient, and absorption coefficient are interconnected with the electronic structure and optical properties of a material. The refractive index is influenced by factors such as the density of the material, changes in composition, impurities, and defects. Modifying the oxygen content can lead to changes in the material's electronic structure, thus affecting its optical properties. The refractive index NiO_x films show only a slight change corresponding to the oxygen content, with no significant influence from the oxygen stoichiometry. Notably, among the NiO_x film samples, the film with intermediate oxygen content ($\text{NiO}_{1.07}$) shows a relatively higher refractive index compared to the other samples. This observation aligns with surface morphology, where the film's appearance transitions from uniform and closely packed small grains to a rough surface characterized by triangular and larger grains. This change in the surface appearance might suggest a decrease in the film density as the oxygen content decreases, contributing to a change in the refractive index.⁴⁸

The refractive index at 2 eV (630 nm) for the films with the highest oxygen content exhibits nearly similar values, while the film with intermediate oxygen content experiences a slight increase. As the oxygen content decreases further, the refractive index decreases accordingly. The observed higher increases in the refractive index for the film with intermediate oxygen content may be attributed to its better crystallinity, contributing to

improved optical properties. On the other hand, the observed decrease in the refractive index for higher oxygen content could result from the structural defects and broadening of peaks observed in the XRD analysis. These defects may be induced by an excess of oxygen in the films.⁴⁹ NiO generally has a low and nearly zero extinction coefficient, indicating minimum light absorption. It is observed that varying the oxygen content does not lead to a significant change in the extinction coefficient as well. The bandgap energy of the NiO_x samples is estimated by analyzing the plot of the absorption coefficient versus photon energy. The bandgap energy value corresponds to the point where a significant increase in the absorption coefficient occurs, indicating the onset of band-to-band transition. The nature of the bandgap in the material is determined by its electronic band structure, which, in turn, is influenced by the crystal structure and chemical composition. In the case of NiO with a rock salt crystal structure, with a relatively wide bandgap, its electronic structure is strongly influenced by the hybridization between the Ni 3d⁸ and O 2p⁶ orbitals, as well as the strong Coulomb interaction among the Ni 3d electrons. Extensive theoretical and experimental studies have already investigated the electronic band structure of NiO in more detail.^{50–52} In this study, the estimated bandgap of NiO_x , as defined by the oxygen composition, indicates that the oxygen content does not significantly affect the bandgap of NiO_x . There is only a slight change observed in the direct bandgap of NiO_x when the oxygen content is varied. This observation could be attributed to the presence of oxygen vacancies or other available defects in the material. These defects may trap electrons or holes, making them unavailable for the band-to-band transitions and resulting in the alteration of the effective bandgap.

18 March 2024 15:19:20

V. CONCLUSIONS

NiO thin films were synthesized using pulsed dc reactive magnetron sputtering with different oxygen flow ratios (4%, 19%, 27%, 35%, 43%, and 51%) and corresponding changes in the oxygen content. Cubic NiO_x is obtained on both Si(100) and c-Al₂O₃ substrates with dominant 111 orientation. On the Si(100) substrate, the NiO_x films exhibited fiber-textured growth, with the [111] direction being orthogonal to the substrate surface. On the c-Al₂O₃ substrate, epitaxially grown NiO_x films were observed with epitaxial relationships of NiO(111) || Al₂O₃(0001) and NiO[110] || Al₂O₃[1010] or NiO[110] || Al₂O₃[2110].

The morphology of the film was also affected by the variation in the oxygen content. The films exhibited changes from rough pyramidal shapes to smooth and uniform surfaces with distinct grain boundaries on both substrates as the oxygen content changed. However, the optical properties of the films, including the refractive index, extinction coefficient, and absorption, were not influenced by the oxygen composition in the film.

ACKNOWLEDGMENTS

This work was supported financially by the Swedish Government Strategic Research Area in Materials Science on Functional Materials at Linköping University (Faculty Grant SFO-Mat-LiU No. 2009 00971), the Knut and Alice Wallenberg Foundation through the Wallenberg Academy Fellows Program (No. KAW-2020.0196), the Swedish Research Council (VR) under Project No. 2021-03826, and the Swedish Energy Agency under Project No. 46519-1. Financial support for the operation of the accelerator laboratory in Uppsala by VR-RFI (Contract No. 2019-00191) and the Swedish Foundation for Strategic Research (SSF, Contract No. RIF14-0053) is gratefully acknowledged.

AUTHOR DECLARATIONS

Conflict of Interest

The authors have no conflicts of interest to disclose.

Author Contributions

Faezeh A. F. Lahiji: Conceptualization (equal); Data curation (equal); Formal analysis (equal); Investigation (equal); Methodology (equal); Software (equal); Visualization (equal); Writing – original draft (equal); Writing – review & editing (equal). **Samiran Bairagi:** Formal analysis (equal); Investigation (equal); Validation (equal); Writing – review & editing (equal). **Roger Magnusson:** Conceptualization (equal); Formal analysis (equal); Software (equal); Writing – review & editing (supporting). **Mauricio A. Sortica:** Formal analysis (supporting); Software (supporting); Writing – review & editing (supporting). **Daniel Primetzhofer:** Data curation (supporting); Formal analysis (supporting); Software (supporting); Writing – review & editing (supporting). **Erik Ekström:** Conceptualization (supporting); Investigation (supporting); Writing – review & editing (supporting). **Biplab Paul:** Conceptualization (supporting); Investigation (supporting); Writing – review & editing (supporting). **Arnaud le Febvrier:** Conceptualization (lead); Data curation (equal);

Methodology (equal); Project administration (equal); Supervision (lead); Validation (equal); Writing – review & editing (lead). **Per Eklund:** Conceptualization (lead); Funding acquisition (lead); Project administration (lead); Supervision (lead); Validation (equal); Visualization (lead).

DATA AVAILABILITY

The data that support the findings of this study are available from the corresponding authors upon reasonable request.

REFERENCES

- ¹S. Ekeröth, S. Ikeda, R. Boyd, P. Mürger, T. Shimizu, and U. Helmerson, *J. Nanopart. Res.* **21**, 1 (2019).
- ²Y. Ichiyanagi, N. Wakabayashi, J. Yamazaki, S. Yamada, Y. Kimishima, E. Komatsu, and H. Tajima, *Phys. B* **329–333**, 862 (2003).
- ³M. Tadic, D. Nikolic, M. Panjan, and G. R. Blake, *J. Alloys Compd.* **647**, 1061 (2015).
- ⁴J. Y. Zhang *et al.*, *J. Mater. Chem. C* **6**, 2275 (2018).
- ⁵M. A. Guziewicz, J. A. Grochowski, M. I. Borysiewicz, and E. L. Kaminska, *Optica Applicata* **XLI**, 201 (2011).
- ⁶W. L. Jang, Y. M. Lu, W. S. Hwang, T. L. Hsiung, and H. P. Wang, *Appl. Phys. Lett.* **94**, 1 (2009).
- ⁷G. Parravano, *J. Chem. Phys.* **23**, 5 (1955).
- ⁸W. Shin and N. Murayama, *Mater. Lett.* **45**, 302 (2000).
- ⁹J. W. Fergus, *J. Eur. Ceram. Soc.* **32**, 525 (2012).
- ¹⁰H. L. Chen, Y. M. Lu, and W. S. Hwang, *Surf. Coat. Technol.* **198**, 138 (2005).
- ¹¹B. Subramanian, M. Mohamed Ibrahim, V. Senthikumar, K. R. Murali, V. Vidhya, C. Sanjeeviraja, and M. Jayachandran, *Phys. B* **403**, 4104 (2008).
- ¹²H. L. Lu, G. Scarel, M. Alia, M. Fanciulli, S. J. Ding, and D. W. Zhang, *Appl. Phys. Lett.* **92**, 2006 (2008).
- ¹³P. Zhai *et al.*, *Chem. Commun.* **50**, 1854 (2014).
- ¹⁴D. Soo Kim and H. Chul Lee, *J. Appl. Phys.* **112**, 1 (2012).
- ¹⁵A. G. Gavriluk, I. A. Trojan, and V. V. Struzhkin, *Phys. Rev. Lett.* **109**, 1 (2012).
- ¹⁶Sani Garba Danjuma, *Int. J. Eng. Res.* **V8**, 461 (2019).
- ¹⁷G. A. Niklasson and C. G. Granqvist, *J. Mater. Chem.* **17**, 127 (2007).
- ¹⁸R. T. Wen, C. G. Granqvist, and G. A. Niklasson, *Adv. Funct. Mater.* **25**, 3359 (2015).
- ¹⁹H. Sato, T. Minami, S. Takata, and T. Yamada, *Thin Solid Films* **236**, 27 (1993).
- ²⁰M. D. Irwin, D. B. Buchholz, A. W. Hains, R. P. H. Chang, and T. J. Marks, *Proc. Natl. Acad. Sci. U.S.A.* **105**, 2783 (2008).
- ²¹I. Hotovy, V. Rehacek, P. Siciliano, S. Capone, and L. Spiess, *Thin Solid Films* **418**, 9 (2002).
- ²²I. Hotovy, J. Huran, L. Spiess, S. Hascik, and V. Rehacek, *Sens. Actuators, B* **57**, 147 (1999).
- ²³H. Shima, F. Takano, H. Akinaga, Y. Tamai, I. H. Inoue, and H. Takagi, *Appl. Phys. Lett.* **91**, 2005 (2007).
- ²⁴X. Kang, J. Guo, Y. Gao, S. Ren, W. Chen, and X. Zhao, *Appl. Surf. Sci.* **480**, 57 (2019).
- ²⁵J.-W. Park, J.-W. Park, K. Jung, M. K. Yang, and J.-K. Lee, *J. Vac. Sci. Technol. B* **24**, 2205 (2006).
- ²⁶Y. Ahn and J. Y. Son, *Ceram. Int.* **47**, 9342 (2021).
- ²⁷H. Y. Peng, Y. F. Li, W. N. Lin, Y. Z. Wang, X. Y. Gao, and T. Wu, *Sci. Rep.* **2**, 1 (2012).
- ²⁸R. S. Kate, S. C. Bulakhe, and R. J. Deokate, *J. Electron. Mater.* **48**, 3220 (2019).
- ²⁹A. Boukhachem, R. Boughalmi, M. Karyaoui, A. Mhamdi, R. Chtourou, K. Boubaker, and M. Amlouk, *Mater. Sci. Eng. B* **188**, 72 (2014).
- ³⁰M. Tyagi, M. Tomar, and V. Gupta, *Adv. Mat. Res.* **488–489**, 103 (2012).
- ³¹Y. Ashok Kumar Reddy, A. Sivasankar Reddy, and P. Sreedhara Reddy, *J. Alloys Compd.* **583**, 396 (2014).

18 March 2024 15:19:20

- ³²M. Wang, Y. Thimont, L. Presmanes, X. Diao, and A. Barnabé, *Appl. Surf. Sci.* **419**, 795 (2017).
- ³³T. Maruyama and S. Arai, *Sol. Energy Mater. Sol. Cells* **30**, 257 (1993).
- ³⁴A. E. Jiménez-González and J. G. Cambray, *Surf. Eng.* **16**, 73 (2000).
- ³⁵I. Bouessay, A. Rougier, B. Beaudoin, and J. B. Leriche, *Appl. Surf. Sci.* **186**, 490 (2002).
- ³⁶D. J. Yun and S. W. Rhee, *J. Vac. Sci. Technol. B* **26**, 1787 (2008).
- ³⁷I. Porqueras and E. Bertran, *Thin Solid Films* **398–399**, 41 (2001).
- ³⁸D. T. Nguyen, A. Ferrec, J. Keraudy, M. Richard-Plouet, A. Goullet, L. Cattin, L. Brohan, and P. Y. Jouan, *Surf. Coat. Technol.* **250**, 21 (2014).
- ³⁹H. W. Ryu, G. P. Choi, W. S. Lee, and J. S. Park, *J. Mater. Sci.* **39**, 4375 (2004).
- ⁴⁰A. Agrawal, H. R. Habibi, R. K. Agrawal, J. P. Cronin, D. M. Roberts, R. Caron-Popowich, and C. M. Lampert, *Thin Solid Films* **221**, 239 (1992).
- ⁴¹D. H. Kwon, S. R. Lee, Y. S. Choi, S. B. Son, K. H. Oh, K. Char, and M. Kim, *Rapid Res. Lett.* **11**, 3 (2017).
- ⁴²S. Seo *et al.*, *Appl. Phys. Lett.* **85**, 5655 (2004).
- ⁴³A. le Febvrier, L. Landalv, T. Liersch, D. Sandmark, P. Sandstrom, and P. Eklund, *Vacuum* **187**, 1–17, (2020).
- ⁴⁴P. Ström and D. Primetzhofer, *J. Instrum.* **17**, P04011 (2022).
- ⁴⁵P. Ström, P. Petersson, M. Rubel, and G. Possnert, *Rev. Sci. Instrum.* **87**, 103303 (2016).
- ⁴⁶G. Bei München and M. Mayer, *SIMNRA User's Guide* (Max-Planck-Institut für Plasmaphysik, 1997).
- ⁴⁷P. Makula, M. Pacia, and W. Macyk, *J. Phys. Chem. Lett.* **9**, 6814 (2018).
- ⁴⁸A. Le Febvrier *et al.*, *ACS Appl. Mater. Interfaces* **4**, 5227 (2012).
- ⁴⁹J.-W. Park, K. N. Choi, S. H. Baek, K. S. Chung, and H. Lee, *J. Korean Phys. Soc.* **52**, 1868 (2008).
- ⁵⁰J. Hugel and M. Belkhir, *Solid State Commun.* **73**, 159 (1990).
- ⁵¹M. Emam-Ismail, M. El-Hagary, H. M. El-Sherif, A. M. El-Naggar, and M. M. El-Nahass, *Opt. Mater.* **112**, 110763 (2021).
- ⁵²J. Feinleib and D. Adler, *Phys. Rev. Lett.* **21**, 1010 (1968).
- ⁵³See supplementary material online for the evolution of the lattice parameter and different representations of the variation of the optical properties.